1-1-2013

Crystallization, phase evolution and ferroelectric properties of sol-gel-synthesized Ba(Ti0.8Zr0.2)O3- x(Ba0.7Ca0.3)TiO3 thin films

Zeng-mei Wang
Southeast University

Kuan Zhao
Southeast University

Xin-li Guo
Southeast University

Wei Sun
Southeast University

Hua-long Jiang
Shandong University

See next page for additional authors

Crystallization, phase evolution and ferroelectric properties of sol-gel-synthesized Ba(Ti0.8Zr0.2)O3- x(Ba0.7Ca0.3)TiO3 thin films

Abstract

A lead-free piezoelectric material with ultra-high properties, Ba(Ti0.8Zr0.2)O3-x(Ba0.7Ca0.3)TiO3(BZT-xBCT) nanocrystals was synthesized via a sol-gel method, and the corresponding thin films were also deposited on Pt/Ti/SiO2/Si substrates by a spin-coating approach. The BZT-xBCT thin film exhibited a high remnant polarization of 22.15 mC cm2 with a large coercive field of 68.06 kV cm1. The resultant gel is calcined at various elevated temperatures and studied with FTIR/XRD/Raman/DSC-TGA/AFM/SEM techniques for gel composition, crystallization, phase transition, thermochemistry and the morphology of the film. Although the room temperature crystal structure of the BZT-xBCT nanocrystals appears to be a standard perovskite structure by conventional X-ray diffraction (XRD), Raman spectroscopy demonstrates the presence of non-centrosymmetric regions arising from the off-centering of the titanium (zirconium) atoms. The Raman spectra findings demonstrate the degree by which the tetragonal phase grows with the increase of calcining temperature in BZT-0.5BCT, and the characteristic ferroelectric-ferroelectric phase transition in BZT-xBCT while going through the MPB process. The structural and constituent evolution for the conversion process from gel to ceramic, as well as the formation mechanism of the BZT-0.5BCT crystallite, were also elucidated.

Keywords

gel, synthesized, ba, ti0, 8zr0, 2, crystallization, o3, ferroelectric, x, ba0, 7ca0, 3, tio3, thin, films, evolution, phase, properties, sol

Disciplines

Engineering | Physical Sciences and Mathematics

Publication Details

Wang, Z., Zhao, K., Guo, X., Sun, W., Jiang, H., Han, X., Tao, X., Cheng, Z., Zhao, H., Kimura, H., Yuan, G., Yin, J. & Liu, Z. (2013). Crystallization, phase evolution and ferroelectric properties of sol-gel-synthesized Ba(Ti0.8Zr0.2)O3- x(Ba0.7Ca0.3)TiO3 thin films. Journal of Materials Chemistry C, 1 522-530.

Authors

Zeng-mei Wang, Kuan Zhao, Xin-li Guo, Wei Sun, Hua-long Jiang, Xue-qin Han, Xu-tang Tao, Zhen-xiang Cheng, Hong-yang Zhao, Hideo Kimura, Guo-liang Yuan, Jiang Yin, and Zhi-guo Liu

Journal of Materials Chemistry C

RSC Publishing

PAPER

View Article Online
View Journal | View Issue

Cite this: J. Mater. Chem. C, 2013, 1, 522

Crystallization, phase evolution and ferroelectric properties of sol–gel-synthesized $Ba(Ti_{0.8}Zr_{0.2})O_3$–$x(Ba_{0.7}Ca_{0.3})TiO_3$ thin films

Zeng-mei Wang,*[ab] Kuan Zhao,[c] Xin-li Guo,[a] Wei Sun,[a] Hua-long Jiang,[a] Xue-qin Han,[a] Xu-tang Tao,[b] Zhen-xiang Cheng,[d] Hong-yang Zhao,[ef] Hideo Kimura,[e] Guo-liang Yuan,[g] Jiang Yin[h] and Zhi-guo Liu[h]

A lead-free piezoelectric material with ultra-high properties, $Ba(Ti_{0.8}Zr_{0.2})O_3$–$x(Ba_{0.7}Ca_{0.3})TiO_3$(BZT–xBCT) nanocrystals was synthesized *via* a sol–gel method, and the corresponding thin films were also deposited on Pt/Ti/SiO_2/Si substrates by a spin-coating approach. The BZT–xBCT thin film exhibited a high remnant polarization of 22.15 μC cm^{-2} with a large coercive field of 68.06 kV cm^{-1}. The resultant gel is calcined at various elevated temperatures and studied with FTIR/XRD/Raman/DSC-TGA/AFM/SEM techniques for gel composition, crystallization, phase transition, thermochemistry and the morphology of the film. Although the room temperature crystal structure of the BZT–xBCT nanocrystals appears to be a standard perovskite structure by conventional X-ray diffraction (XRD), Raman spectroscopy demonstrates the presence of non-centrosymmetric regions arising from the off-centering of the titanium (zirconium) atoms. The Raman spectra findings demonstrate the degree by which the tetragonal phase grows with the increase of calcining temperature in BZT–0.5BCT, and the characteristic ferroelectric–ferroelectric phase transition in BZT–xBCT while going through the MPB process. The structural and constituent evolution for the conversion process from gel to ceramic, as well as the formation mechanism of the BZT–0.5BCT crystallite, were also elucidated.

Received 22nd August 2012
Accepted 25th September 2012

DOI: 10.1039/c2tc00020b

www.rsc.org/materialsC

Introduction

Piezoelectric materials are an important class of functional materials that generate a voltage in response to mechanical strain (and *vice versa*). During the past 50 years, lead zirconate titanate PZT ceramics, exhibiting outstanding piezoelectric performance (d_{33} = 220–590 pC N^{-1}), have been central to a vast range of applications.[1,2] Unfortunately, they are now facing global restrictions in their usage because of lead oxide toxicity. Therefore, the study of lead-free piezoelectric ceramics that can compete with the PZT family has been an urgent demand in the world.[3–5] It has led to immense achievements in the preparation of high performance ferroelectrics, especially piezoelectric materials.[6] $BaTiO_3$-based ceramics are one kind of important lead-free piezoelectric ceramics due to their outstanding dielectric and ferroelectric properties; for instance, barium calcium titanate (BCT),[7] barium zirconate titanate (BZT),[8] barium strontium titanate (BST) piezoelectric ceramics,[9] and so on. However, these materials still do not exhibit very high piezoelectricity or ferroelectricity compared with PZT.

Fortunately, a recent report showed a high piezoelectric coefficient up to 620 pC N^{-1} in bulk ceramics with a perovskite structure and a complex composition of $0.5Ba(Ti_{0.8}Zr_{0.2})O_3$–$0.5(Ba_{0.7}Ca_{0.3})TiO_3$ (BZT–0.5BCT).[10] It was thought that the strong piezoelectric effect may stem from a morphotropic phase boundary (MPB) starting from a tetragonal–cubic–rhombohedral triple point, which causes a very low energy barrier for polarization rotation and lattice distortion. The results aroused wide concern in the field of lead-free materials and some further research has been performed on this material system from then on.[11–15]

Implementation of a lead-free thin film with a strong piezoelectric effect is requested for many micro-systems, and it is interesting to fabricate perovskite BZT–xBCT thin films.

[a]School of Materials Science and Engineering, Key laboratory of Construction Materials, Southeast University, Nanjing 211189, P. R. China. E-mail: zmwangster@gmail.com; Tel: +86-25-52090668
[b]State Key laboratory of Crystal Materials, Shandong University, Jinan 250100, P. R. China
[c]Department of Physics, Southeast University, Nanjing, 211189, P. R. China
[d]Institute for Superconducting and Electronic Materials, University of Wollongong, Innovation Campus, Fairy Meadow, NSW 2519, Australia
[e]National Institute for Materials Science (NIMS), Segen 1-2-1, Tsukuba, 305–0047, Japan
[f]Shanghai Institute of Ceramics, Chinese Academy of Sciences, Shanghai, China
[g]School of Materials Science and Engineering, Nanjing University of Science and Technology, Nanjing, 210094, P. R. China
[h]Department of Materials Science and Engineering, National Laboratory of Solid State Microstructure, Nanjing University, Nanjing, 210093, P. R. China

Currently, most ferroelectric ceramic thin films can be deposited on platinum silicon substrates, Pt(111)/Ti/SiO_2/Si(100), with the composition near the morphotropic phase boundary by the sol–gel or chemical solution deposition method, sputtering pulsed laser ablation, and metal–organic chemical vapor deposition. Chemical solution deposition (CSD) and particularly sol–gel processing offers some advantages in terms of low temperature preparation, composition homogeneity, the possibility of covering a large substrate area, cost-effectiveness, and processing simplicity, when compared with the other methodologies, namely, physical deposition methods. Nowadays, there are some reports concerning the fabrication of BZT–*x*BCT thin films.[16–18] Most are focused on the excellent piezoelectric properties and the structure–properties relationship of this system. For CSD, especially sol–gel methods, understanding the individual reaction step of the transformation from the mixture of starting materials to BZT–*x*BCT nanoparticles or the corresponding films is very important for controlling the physical properties of the final products. Although several investigations have been done on the reaction mechanisms of $BaTiO_3$,[19–22] these conclusions are inadequate and even conflicting each other, and the mechanism of $BaTiO_3$ formation from metal organic precursors is not yet well understood.

In the present experiment, we try to prepare a series of different stoichiometric compositions of BZT–*x*BCT ferroelectric powders across MPB by the sol–gel technique, and particularly investigate the phase evolution and detailed chemical changes of BZT–0.5BCT during the xerogel to ceramic phase change by thermal analysis, Fourier transform infrared analysis (FTIR), X-ray diffraction (XRD), and Raman spectrum measurements. Finally, BZT–*x*BCT polycrystalline ferroelectric thin films were also obtained on Pt-coated silicon substrates by the spin-coating method.

The main goal of this paper is to investigate the possible reaction mechanism of barium acetate [$Ba(CH_3COO)_2$] and calcium acetate monohydrate [$Ca(CH_3COO)_2\cdot H_2O$] with tetrabutyl titanate [$Ti(OC_4H_9)_4$], and zirconium oxynitrate [$ZrO(NO_3)_2\cdot 2H_2O$] during the formation of crystalline BZT–*x*BCT using the sol–gel method, and to provide some available controllable factors to get high quality ferroelectric thin films.

Experimental section

The starting materials of barium acetate [$Ba(CH_3COO)_2$], calcium acetate monohydrate [$Ca(CH_3COO)_2\cdot H_2O$], tetrabutyl titanate [$Ti(OC_4H_9)_4$], and zirconium oxynitrate [$ZrO(NO_3)_2\cdot 2H_2O$] were all of analytical grade and were used without further purification. Glacial acetic acid and absolute alcohol were employed as the chelating agent and solvent, respectively. Deionized water was used in all experimental techniques. In a precursor synthesis, Ba–Ca, and Ti–Zr solutions were separately produced. Solution A was prepared by dissolving stoichiometric $Ba(CH_3COO)_2$ and $Ca(CH_3COO)_2\cdot H_2O$ in a mixed solution of acetic acid and deionized water, and then stirring for 1 h to form Ba–Ca solution. For solution B, to suppress the hydrolysis of $Ti(OC_4H_9)_4$, an appropriate amount of glacial acetic acid was first added to the accurately weighed $Ti(OC_4H_9)_4$, stirring for 20 min, followed by adding $ZrO(NO_3)_2\cdot 2H_2O$ and absolute alcohol, and stirring at room temperature for 1 h to form Ti–Zr solution. Finally, solution A was added into solution B with stirring for 2.5 h at room temperature, and then maintained at 40–50 °C for about 1 h to obtain a clear and homogeneous gel.

Thin films were prepared by spin-coating the above solution at 800 rpm for 9 s and at 3000 rpm for 30 s on clean platinum-coated silicon substrates. The spin-coated films were heat-treated at 140 °C for 10 min and pyrolyzed at 450 °C for 20 min for each deposited layer. This cycle was repeated in order to get films with a final thickness around 800 nm. The films were annealed for 1 h at 850 °C in an air atmosphere. The preparation procedure is briefly summarized in Fig. 1.

To study the solution chemical and phase evolution process of the precursor, the BZT–0.5BCT gel was heat-treated at different temperatures, 150, 200, 320, 400, 480, 540, 600, 650, 700, 750, 850, and 950 °C for 0.5 h in air atmosphere in a muffle furnace. BZT–*x*BCT ($x = 0.3$, 0.4, 0.45, 0.5, 0.55, 0.6, 0.7, 0.8, 0.9, 1.0) gels were also heat-treated at 950 °C for 2.5 h to study the phase evolution going through the MPB.

The chemical decomposition evolution of the BZT–0.5BCT gel series was examined with the Fourier transform infrared (FTIR) spectroscopic method (the KBr pellet technique) for its characteristic IR absorption bands. The FTIR spectra of the samples were recorded with a 2 cm^{-1} resolution on a computerized FTIR spectroscope (Nicolet 5700). Typically, 1.2 mg of the finely ground gel sample was well mixed with 10 equivalents of dry spectroscopic grade KBr powder in a dry environment. The mixture was then pressed in a die to produce a transparent pellet. The crystallographic information on the above gel series was established by using the XRD method and Raman spectra. The diffraction intensity 2θ spectra were measured in a Bruker AXS D8 DISCOVER with Cu K_α radiation ($\lambda = 1.5418$ Å) in a 2θ range of 10–90° at a scanning rate of 9° min^{-1}. A Horiba Jobin Yvon LabRAM HR UV-Visible Raman system was used to obtain Raman spectra, employing a laser excitation wavelength of 514 nm. Thermal behaviors of the BZT–0.5BCT gel were studied by thermogravimetry (TG) and differential scanning calorimetry (DSC), which were performed on a Netzsch STA449 F3 in an air atmosphere. The temperature was scanned from room temperature to 1200 °C at a heating rate of 10 °C min^{-1}.

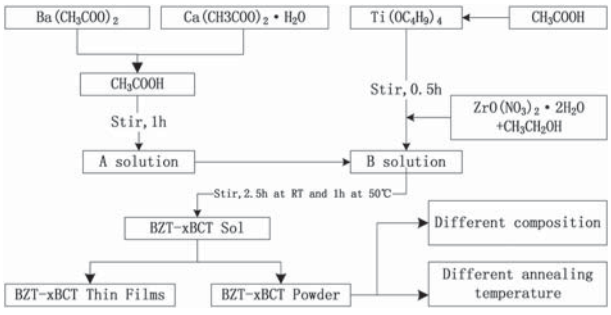

Fig. 1 Flow chart of the preparation process for BZT–*x*BCT thin films and powder.

The surface morphology and thickness of the BZT–xBCT films were evaluated by atomic force microscopy (AFM, Digital Instrument, Nanoscope III) and field emission scanning electron microscopy (FESEM, FEI, XL30). For characterization of the ferroelectric properties, platinum electrodes ($\phi = 0.1$ mm) were sputtered on the surface of the film using a shadow mask to form metal–insulator–metal (MIM) capacitors. The P–E hysteresis loops were measured using a tester of ferroelectric analysis (PremierII, Radiant Technologies). All the measurements were performed at room temperature.

Results and discussion

Chemical constituents of BZT–0.5BCT gels

The FTIR spectral evolution of the dried xerogel at different calcined temperatures is reported in Fig. 2. For the low temperature calcined samples (150 °C and 200 °C), the absorption peaks at 1565 and 1415 cm^{-1} correspond to the carboxyl group asymmetric $\nu_{as}(COO^-)$ and symmetric $\nu_s(COO^-)$ stretching vibrations of the acetate ligands. The difference in frequency $\Delta\nu$ between the asymmetric and symmetric vibrations of the COO^- bonds is usually related to the type of carboxylate coordination.[23] The frequency separation ($\Delta\nu$) between the two peaks strongly depends on the bonding mode, such as the largest ($\Delta\nu = 425$ cm^{-1}) in the monodentate ligand and the smallest ($\Delta\nu = 130$–80 cm^{-1}) in the chelating one. The bridging acetate groups have an intermediate value ($\Delta\nu = 140$–160 cm^{-1}) which is slightly larger than that of the chelating mode. Therefore, the frequency separation, $\Delta\nu$ (150 cm^{-1}), between $\nu_{as}(COO^-)$ at 1565 cm^{-1} and $\nu_s(COO^-)$ at 1415 cm^{-1} suggests that the acetate ligands both coordinate to titanium in bridging mode (with $\Delta\nu$ between 140 and 160 cm^{-1}). It should be mentioned that the addition of acetic acid molecules is essential during the sol preparation. Without it, the hydrolysis of $Ti(OR)_4$ will occur vigorously, resulting in precipitates of titania. The absorption peaks at 1388 cm^{-1} are assigned to overlap of the $-CH_3$ vibration modes and nitrate ion, NO_3^{-1}, remaining in the gels.[24] The C–C skeletal stretching mode at 945 cm^{-1} can be clearly identified for the low-temperature calcined samples.[25,26] The C═O vibration modes can be observed at 848, 825, and 1020 cm^{-1}, respectively[27] and the peak at 1050 cm^{-1} is assigned to the –C–O–C– stretching mode. These hydrocarbon species reflect the fact that below 200 °C, certain organic compounds are still retained or encapsulated in the amorphous gel. The band around 787 cm^{-1} can be attributed to the FT-IR spectra of barium oxalate ($Ba(C_2O_4)$). Therefore, it is clear that $Ba(C_2O_4)$ is generated at temperatures lower than 200 °C by thermal decomposition of unreacted $Ba(OAc)_2$, leading to the loss of methyl groups ($-CH_3$). In addition, the band around 787–620 cm^{-1} appears which might be assigned to the Ti–O–Ti linkage formation by expanding the coordination of Ti; this indicates that acetic acid is completely effectively stabilizing this alkoxide. The bands between 700 and 400 cm^{-1} are mainly attributed to the formation of metal oxides (M–O: Ba–O, Ca–O, Ti–O and Zr–O). The peak corresponding to $Ti(-OR)_4$ (around 1137 cm^{-1}) was not detected, indicating that the alkoxy groups of $Ti(OC_4H_9)_4$ are not present and are completely removed when acetic acid is used.

When the gel is sintered above 320 °C, the characteristic bands of COO^- at 1565 cm^{-1} and 1428 cm^{-1} merge into a single broad band ranging from 1200 cm^{-1} to 1600 cm^{-1}. Within this absorption band, two weak absorption bands at 1428 cm^{-1} and 860 cm^{-1} reveal CO_3^{2-}, meaning the existence of $BaCO_3$ and

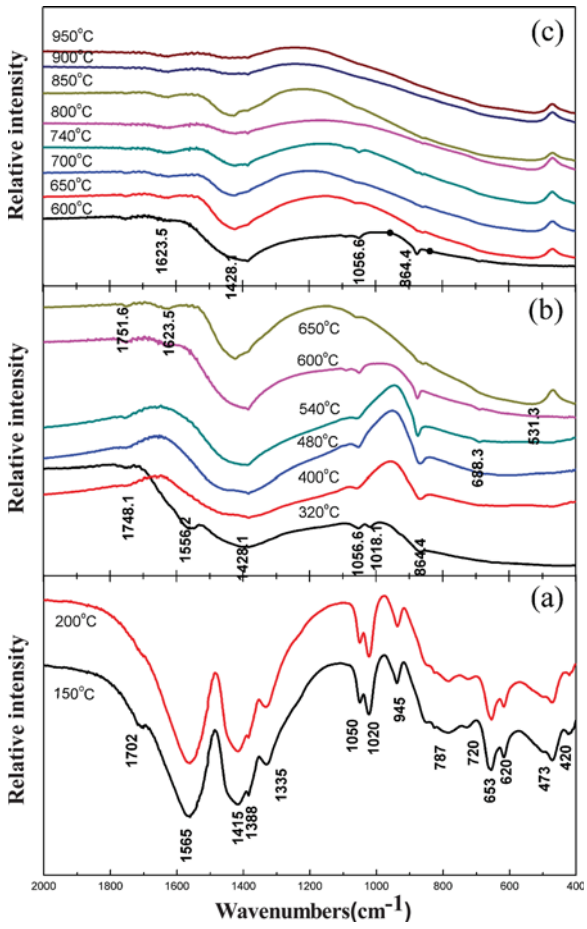

Fig. 2 FTIR spectra recorded for the different heat treated gels. (a) 150–500 °C; (b) 320–650 °C; (c) 600–950 °C.

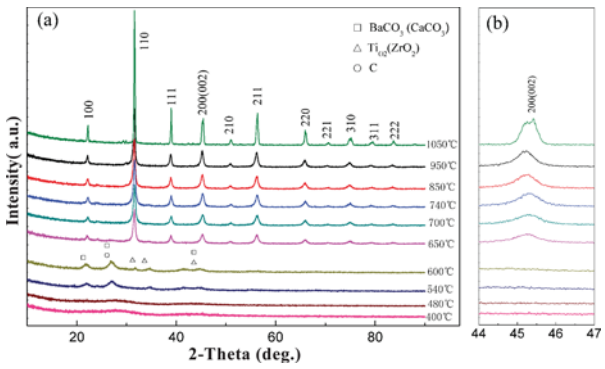

Fig. 3 (a) XRD patterns of BZT–0.5BCT gel calcined at different temperatures; a possible secondary phase is also marked on the graph; (b) narrow-range XRD patterns indicating the position of cubic-phase (200) reflections and the growth of a tetragonal phase.

$CaCO_3$. Also, the absorption band of carbonaceous substances are at about 1600 cm^{-1} and 1360 cm^{-1}. The peaks of CO_3^{2-} and carbonaceous substances overlap each other and make one broad absorption band. Carbonate (CO_3^{2-}) and carbonaceous substances are the combustion products of oxalate ($Ba(C_2O_4)$, $Ca(C_2O_4)$). The sample's color change with temperature also supported this fact, as it changed from black (320–540 °C) to grey (600–650 °C) to white (above 700 °C). With increasing temperature , the absorption of trace $BaCO_3$, $CaCO_3$ and carbonaceous substances becomes weaker and weaker. The characteristic vibration frequency of metal oxides between 400 and 700 cm^{-1} disappeared, indicating that the Ti–O–Zr–O–Ti– network was destroyed to some fragments with the heat-treatment process, which was in line with the amorphous phase in XRD shown in Fig. 3. No apparent absorption peaks for other organic substances can be found, even when the temperature is as low as 400 °C. When the temperature reaches up to 650 °C, the broad and strong absorption band at around 530 cm^{-1} becomes pronounced, which can be assigned to Ti–O stretching normal vibrations of TiO_6 octahedra. This implies that the samples begin to become crystalline, which agrees well with the XRD results shown in Fig. 3.

Structure and phase transformation of BZT–0.5BCT gel: (a) sintering temperature

To detect the crystal phase evolved in each decomposition step of the xerogel, all samples characterized by XRD here were calcined at various temperatures in air for 0.5 h. As shown in Fig. 3(a), no strong crystal phases can be found from the XRD pattern under 480 °C, meaning that the samples are composed of an amorphous phase. Formation of BZT–0.5BCT starts between 540 and 600 °C and is practically finished at 650 °C. The diffraction pattern collected at 540 and 600 °C shows the peaks of whiterite-$BaCO_3$ ($CaCO_3$) and BZT–BCT, TiO_2 (ZrO_2), and even carbon phases, as marked in the XRD pattern. Other phases (*e.g.* Ba_2TiO_4), if any, are below the XRD detection limit. The XRD results together with the FTIR results imply that $BaCO_3$, $CaCO_3$, TiO_2, and ZrO_2 are the main reactants to form BZT–0.5BCT, *i.e.* the formation of BZT–0.5BCT occurs *via* reactant contact by a core–shell structure[28] and interface structure, which will be discussed later in depth. When the temperature is above 650 °C, the XRD pattern of the BZT–0.5BCT is consistent with a cubic or tetragonal perovskite-structure, and the peaks grow stronger with elevated temperature; simultaneously, the crystal phases of $BaCO_3$ and TiO_2 become lower and lower, until they disappear at about 850 °C in air. The 2θ range between 40° and 50° is commonly used to distinguish the cubic and tetragonal phases, where the single (200) peak characteristic of the cubic structure splits into the two tetragonal peaks, (200) and (002).[29] However, it is difficult to assign the crystal structure of small nanocrystals (NCs) using conventional X-ray diffraction because of the significant line broadening caused by a short coherence length. Despite these difficulties, this range also reveals some interesting findings. The splitting is less distinct for NCs sintered at lower temperature, indicating a gradual change in the average NC structure from cubic to tetragonal as the sintering temperature increases. For the initial formation of BZT–0.5BCT NCs at 650–850 °C, the peak has an asymmetric shape, indicating the existence of tetragonal and cubic phases. This tetragonal structure might partly be a consequence of averaging ⟨111⟩ displacements of octahedral Ti^{4+} (local rhombohedral structure),[30] although these distortions cannot be conclusively identified from the present results. The XRD features show a manifest asymmetry and splitting at 850–950 °C, which is even more pronounced at 1150 °C, as observed in Fig. 3(b), suggesting contributions from the tetragonal phase.

In addition to XRD analysis, which gives an average and static symmetry, the local and dynamic symmetry of the BZT–0.5BCT transition from gel to multicrystalline ceramic was monitored by Raman spectroscopy. Raman spectroscopy is a highly sensitive spectroscopic technique to probe the local atomic structure of materials, and can thus be used to identify the tetragonal or cubic phase structure. The cubic perovskite structure inherently has no Raman active modes, and eight Raman active modes are expected for the noncentrosymmetric tetragonal structure, $3A_{1g} + B_{1g} + 4E_g$.[31] The Raman spectra of the BZT–0.5BCT sintered at different temperatures are shown in Fig. 4. The spectrum of the sample collected at 540 °C is featureless, demonstrating the predominantly amorphous character of the gel. Increasing the sintering temperature to 600 °C leads to the appearance of weak and broad Raman bands of carbonate species ($BaCO_3$ and $CaCO_3$) at 136, 230, 688, 760,

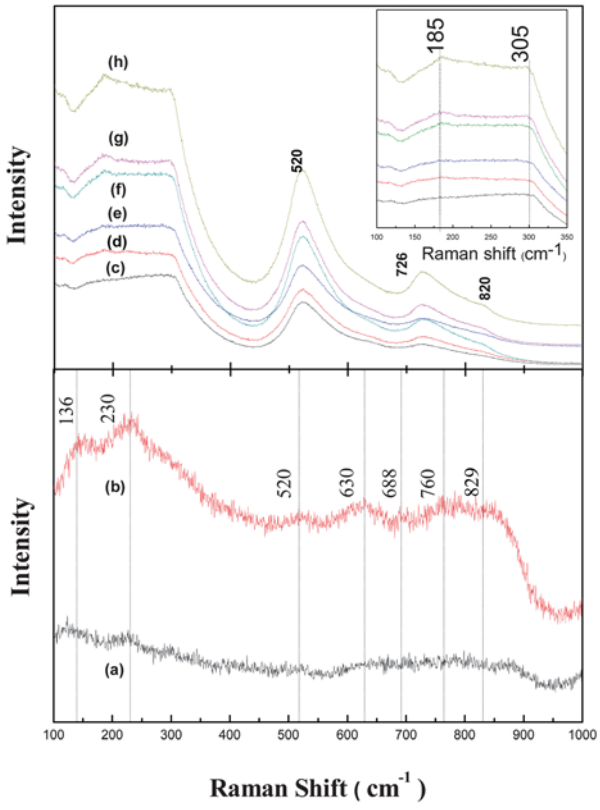

Fig. 4 Raman spectra of BZT–0.5BCT heated to (a) 540 °C, (b) 600 °C, (c) 650 °C, (d) 700 °C, (e) 750 °C, (f) 850 °C, (g) 900 °C, (h) 950 °C.

and 829 cm^{-1} (ref. 32) and bands for anatase occur at 514 and 630 cm^{-1},[33] together with the 520 cm^{-1} band, assigned to BZT–0.5BCT. The characteristic peak of the carbon phase around 1060 cm^{-1} was not detected due to the limits of the measurement range. This observation is in good agreement with the XRD and FTIR data. The peak at 806 cm^{-1} is not an intrinsic mode of tetragonal BZT–0.5BCT. According to Shiratori *et al.*,[34] this peak is associated with the presence of hydroxyl lattice groups, which can reside as defects on oxygen sites within BZT–0.5BCT.

For samples heated to 650 °C, the BZT–0.5BCT bands at 185, 305, 520, and 726 cm^{-1} become prominent, and the very faint band around 630 cm^{-1} is still detected, disappearing at 850 °C. The band at 520 cm^{-1} has been observed in both the cubic and tetragonal phases of BTO and was conclusively assigned to scattering from the fundamental transverse component of the optical (TO) mode of A1 symmetry.[32] Because first-order $Pm\bar{3}m$ Raman scattering is symmetry-forbidden in the centrosymmetric space group, the activation of these phonons has been attributed to the presence of non-centrosymmetric regions in which the titanium (zirconium) atom is displaced from the center of the TiO_6 (ZrO_6) octahedra.[35] The band at about 726 cm^{-1} has been observed in the tetragonal phase of BZT–0.5BCT and is related to the highest frequency longitudinal optical mode (LO) A1 symmetry and E (LO).[36–38] The peak at 305 cm^{-1} attributed to the B1 mode is a characteristic peak for BZT–0.5BCT and indicates the asymmetry of the TiO_6 octahedra.[39,40] This band is considered to be the Raman signature of the tetragonal phase. Therefore, it is possible to investigate how the non-centrosymmetric tetragonal regions develop as the BZT–0.5BCT nanocrystals grow from the amorphous gel. Thus, careful attention was paid to the presence of a peak at ~305 cm^{-1}; expanded spectra for the samples collected at 650–950 °C within the 100–350 cm^{-1} wavenumber range are shown in the inset of Fig. 4. It can be seen that the peak at 305 cm^{-1} becomes sharper and sharper with elevated temperature. This indicates the formation of a higher degree of tetragonal phase during the reaction. The peak around 180 cm^{-1} arises from the coupling of A1(TO) phonons,[32,35,41] and starts to grow at 850 °C and gets more and more pronounced with increasing sintering temperature.

The weak intensity of the vibration bands of the BZT–0.5 BCT gel, as well as their broadness, is typical of heavily damped phonons. Likewise, the presence of a weak peak at ~180 cm^{-1} indicates weak coupling between the A1(TO) phonons. Both observations confirm the reduced structural coherence of the nanocrystals with respect to their single crystal and bulk counterparts. Taken together, the XRD and Raman spectroscopy results indicate the presence of non-centrosymmetric regions that result from the local off-centering of the titanium (zirconium) atoms. Most importantly, in the perspective of this work, is the observation that the coherence of the local displacements of the titanium (zirconium) atoms increases with increasing sintering temperature, ultimately leading to the development of non-centrosymmetric tetragonal (*i.e.* ferroelectric) regions after sintering at 850 °C. This finding is very helpful for the sintering temperature of film counterparts.

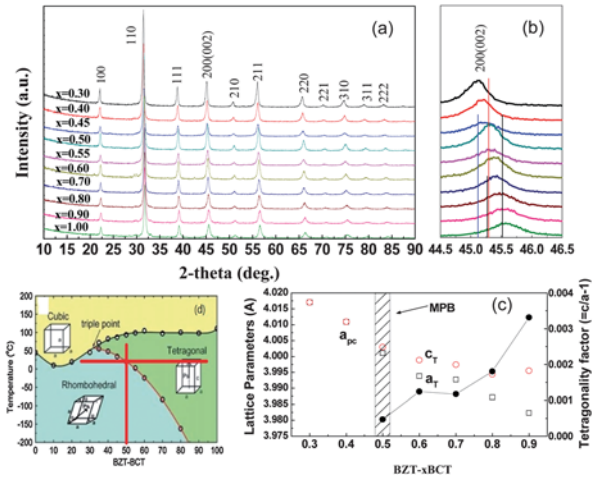

Fig. 5 (a) XRD patterns of BZT–*x*BCT (x = 0.30–1.00). (b) Narrow range (44–46.5°) XRD patterns of BZT–*x*BCT. Vertical blue and red and black lines represent the XRD patterns of cubic, rhombohedral, and tetragonal phases, respectively, and the doping concentrations corresponding to the XRD patterns are indicated in the graphs. The doping concentrations in (b) are the same as those in (a). (c) Lattice parameters and tetragonality factor (c/a − 1). Phase boundary region is indicated by the shaded area. (d) Phase diagram of pseudobinary ferroelectric system BZT–*x*BCT.[10]

Structure and phase transformation of BZT-xBCT gel: (b) composition

According to the phase-diagram of BZT–*x*BCT (established by Liu and Ren[10]), for the composition located in proximity to a ferroelectric–ferroelectric morphotropic phase boundary (MPB) of the system, it exhibits the highest spontaneous polarization, P_m, highest remnant polarization, P_r, lowest coercive field, E_c, and highest dielectric permittivity ε. We study the structure and phase evolution by varying the composition x in BZT–*x*BCT (along the horizontal line in Fig. 5(d)) across the MPB. All the samples show a $BaTiO_3$-like perovskite structure, and the two terminal compounds (BCT and BZT) are characterized by a rhombohedral (R) structure and tetragonal (T) structure, respectively. The lattice parameters (a and c) and tetragonality

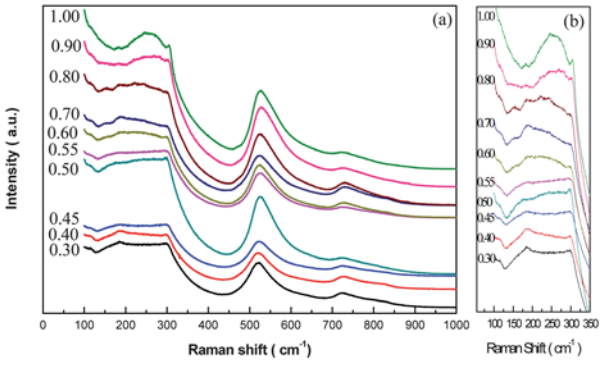

Fig. 6 (a) Raman spectra for different compositions BZT–*x*BCT (x = 0.30–1.00) showing the signature of a transition near x = 0.50, and the spectral feature near 250 cm^{-1} is flat and broad lower than x = 0.50, beginning to grow at x = 0.50 and get more and more stronger subsequently (see also in (b)).

$(c/a - 1)$ as a function of the concentration (x) of tetragonal terminal BCT are shown in Fig. 5(c). With decreasing x, the tetragonal lattice parameters a_T and c_T gradually converge to one pseudo-cubic lattice parameter a_{PC} and the tetragonality decreases to nearly zero at $x = 0.5$, indicating the characteristics at MPB. The influence of the composition of BZT–xBCT (x = 0.30, 0.40, 0.45, 0.50, 0.55, 0.60, 0.70, 0.80, 0.90, 1.00) on the structure can be studied by examining the (200) XRD region (2θ = 44.5–46.5°). With increasing concentration of BCT, the peak shifts to higher angles, along with its broadening and then implies a transformation from R phase to the T phase.

Fig. 6(a) shows Raman spectra of BZT–xBCT (x = 0.30–1.00). Consistent with the XRD results, it shows the signatures of the structure phase transition going through the MPB, and in these samples those are seen as weak features at ~250 cm^{-1}. The band around 250 cm^{-1} is a very weak and broad negative peak for the composition x = 0.3–0.45, and begins to grow at $x = 0.5$, then gets more and more pronounced to form a strong central peak at the terminal BCT composition. Such behavior is well-documented in similar ferroelectric perovskites,[42,43] supporting the existence of a ferroelectric–ferroelectric (rhombohedral–tetragonal) phase transition at about $x = 0.50$ for BZT–xBCT.

Thermal decomposition process

Powders of the white precursor derived from the gel dried at 140 °C were thermally analyzed in simulated air for DSC-TGA with a constant heating rate (10 °C min^{-1}). The TGA curve reveals a first weight loss between RT and 250 °C, with 7.11% losses of total weight, which can be ascribed to the evaporation of the residual non-structural water and solvents. It causes an endothermal peak at 76.6 °C. The second weight loss, according to the XRD results (Fig. 3(a)), is related to a destruction of the xerogel network and the successive loss of organic substances, and the initial formation of BZT–0.5BCT. The consequent four exothermal peaks, at 294.5, 371.1, 431.3 and 510.1 °C, respectively, reveal the combustion reactions and the preliminary synthesis of BZT–0.5BCT by means of $BaCO_3$, $CaCO_3$@TiO_2, ZrO_2 core–shell particles.[28] In agreement, in the XRD pattern, at 540 °C, the BZT–0.5BCT phase can be detected. The last peak at 691.6 °C shows an exothermal effect with 8.67% weight loss. This is attributed to the decomposition of $BaCO_3$, $CaCO_3$ and mechanical mixing with TiO_2, ZrO_2, then reaction to form BZT–0.5BCT. The formation of BZT–0.5BCT is completed at about 767 °C as shown in Fig. 7.

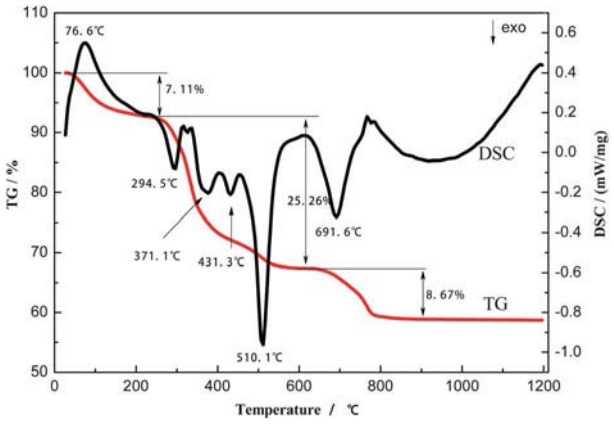

Fig. 7 DSC-TGA analysis for the dried gel (dried at 140 °C) BZT–0.5BCT over room temperature to 1200 °C measured at 10 °C min^{-1} in air atmosphere with a flow rate of 20.0 mL min^{-1}.

Possible mechanism for BZT–xBCT formation

On the basis of the above phase and constituent evolution investigations, and thermal analysis, some interesting features of the chemistry of sol formation and the formation mechanism of the BZT–xBCT crystallite was proposed.

In the sol–gel reaction process, it was shown that the incorporation of acetic acid avoided both the gelation of the reactive medium before the hydrolysis process and the titania precipitation when water was added. Actually, acetic acid is well known to control the hydrolysis rates of highly reactive alkoxides by forming bidentate complexes, more stable than non-chelated or non-bridged ones. Hydrolysis of the –butoxy (the more prone to water attack) and condensation lead to the formation of μ-oxo bridges. In the system under investigation, with addition of acetic acid, $Ti(OC_4H_9)_4$ will form chains upon reaction with a chelating agent of acetic acid (see molecular structure in Fig. 8), in which titanium in a distorted octahedron and all acetate groups act as bridging ligands. The modification of tetrabutyl titanate by acetate was found to saturate at about two acetate groups per titanium atom. This is supported by FTIR results below 200 °C which show the acetate ligands both coordinate to titanium in bridging modes (with $\Delta\nu$ between 140 and 160 cm^{-1}). During the sol–gel reaction of chelated tetrabutyl titanate, the –butoxy groups are preferentially hydrolyzed while the ligands remain tightly bound throughout much of the condensation process, thus promoting the formation of linear chains of Ti–O–Ti polymers composed of edge-sharing octahedra. Also, both the band at around 1650 cm^{-1} of $Ba(CH_3COO)_2$ and $Ca(CH_3COO)_2$ aqueous solution for the monodentate COO^- stretching mode and the band at 1600 cm^{-1} due to the bending vibrations of a Ti–OH bond were not detected, meaning the completion of hydrolysis and condensation at this stage.

The general polycondensation sequence of reaction is as follows:

Hydrolysis:

$$M(OR)_n + xH_2O \rightarrow M(OH)_x(OR)_{n-x} + xROH \quad (1)$$

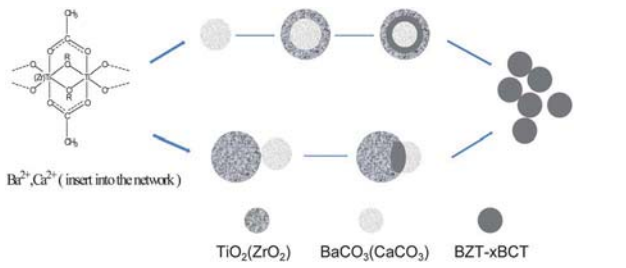

Fig. 8 Schematic representation of the different processes leading to the formation of BZT–0.5BCT nanoparticles in the case of core–shell structures and mechanical mixtures.

Subsequent condensation reactions involving the hydroxyl groups yield networks composed of inorganic oxide (M–O–M) linkages.

Olation:

$$\text{–M–OH + HO–M} \rightarrow \text{–M–O–M + } H_2O \quad (2)$$

$$\text{–M–OH + R–OM} \rightarrow \text{–M–O–M + ROH} \quad (3)$$

During sintering, the –O–Ti–O–Zr–O–Ti– network began to grow, and Ba^{2+} and Ca^{2+} cations were inserted in the network. As the temperature increased to 400–480 °C, the characteristic bands of COO^- at 1565 cm^{-1} and 1415 cm^{-1} are absent and a single broadband range from 1200 cm^{-1} to 1600 cm^{-1} appears. This suggests that the carboxylate combusted with the product of CO_3^{2-} and carbon (supported by the color change of the samples), accompanied by the destruction of the xerogel network. This was evident from the amorphous phase in XRD and Raman spectra, together with the weight loss and endothermic peaks in the DSC-TGA curve before 480 °C.

As the calcination temperature becomes more intense (>540 °C), the TiO_6 octahedra undergo molecular arrangement and phase transformation occurs. X-Ray diffraction (XRD) together with FTIR and Raman results, showed the presence of crystallites of carbonate, which imply the barium (calcium) carbonates are generated at a temperature lower than 600 °C by thermal decomposition of unreacted $Ba(CH_3COO)_2$ or $Ca(CH_3COO)_2$. From these results of XRD and Raman spectra, we propose the following decomposition mechanism for the $Ba(CH_3COO)_2$ or $Ca(CH_3COO)_2$:

$$Ba(OOCCH_3)_2 \xrightarrow{\uparrow CH_3} Ba(OOC)_2 \xrightarrow{\uparrow CO} BaCO_3 \quad (4)$$

These results also can be supported by the variation of the FT-IR spectra for the calcined BZT–0.5BCT precursor. $BaCO_3$ ($CaCO_3$), and TiO_2 (ZrO_2), carbonaceous substances and BZT–0.5BCT phases are present simultaneously at a temperature of 600 °C. No trace of other recognizable intermediate was shown. With elevated calcination temperature, more and more BZT–0.5BCT phases were formed, the phases of $BaCO_3$ ($CaCO_3$), and TiO_2 (ZrO_2) are absent in the sample calcined at 850 °C. Finally, a well-crystallized tetragonal BZT–0.5BCT phase without any secondary phase is obtained at temperatures above 900 °C. From the XRD pattern, the BZT–0.5BCT phase firstly was observed around 540 °C, then gets more and more robust at higher temperature. In agreement, there is one much sharper peak occurring at 510.1 °C in the thermal analysis, and subsequently another weakened peak at 691.6 °C. This implies that the formation of BZT–0.5BCT starts around 500 °C, proceeds rapidly between 600 °C and 650 °C, and is nearly completed at ~650 °C, and the reaction around 600–650 °C is dominant, and the maximum reaction rate can be better appreciated from the TGA curve of the great weight loss (about 510 °C). In contrast, in formation of $BaTiO_3$ by the core–shell structures and mechanical mixtures, there is a single endothermic peak at ~660 °C for the former, and the latter has three DTA peaks at ~650 °C, ~840 °C, and ~930 °C (very faint), respectively.[28] Therefore, there are two possible routes to form crystalline BZT–0.5BCT in our case—in contact with both the core–shell structure and mechanical mixture, and the former is dominant. The BZT–*x*BCT amorphous gel can be described as intermediate that where many Ba^{2+} and less Ca^{2+} ions are inserted into a Ti–O–Zr–O–Ti– polymer network, resembling solids formed by a mixture of reactive titanium (less zirconium) oxide gel with barium and calcium oxide. The role of the ligands primarily is to keep these metal ions in intimate contact. From a more general point of view, the core–shell structures can be obtained by means of such colloidal chemistry,[44] in which the Ti–O–Zr–O– network skeleton acts as the shell, and the cores contain oxalate of barium and calcium. Accompanied by the evaporation and decomposition of non-structural water and organic substances in the thermal treatment, the network becomes fragmented with amorphous phase, and particles of $BaCO_3$ ($CaCO_3$)@TiO_2 (ZrO_2) with a core–shell structure then formed. During this process, some $BaCO_3$ ($CaCO_3$) particles in the fringe will form a mechanical mixture with TiO_2 (ZrO_2).

Taking into account the thermodynamic decomposition of $BaCO_3$ and $CaCO_3$ in air is ~820 °C and 890 °C, respectively.[45] The formation of BZT–*x*BCT from the $BaCO_3$ ($CaCO_3$)@TiO_2 (ZrO_2) particles directly involves solid carbonate without the preliminary decomposition in BaO and CaO and CO_2 according to the solid-state reaction:

$$BaCO_3\ (CaCO_3) + TiO_2\ (ZrO_2) \rightarrow \text{BZT–}x\text{BCT} + CO_2 \quad (5)$$

This reaction occurs between crystalline carbonate and titania (less zirconia), the latter either in amorphous or in nanocrystalline state. This interpretation is strongly supported by the reported results.[46] In core–shell particles, the improved reactivity of the coated particles with respect to the mechanical mixture can be mainly ascribed to the fact that the contact area

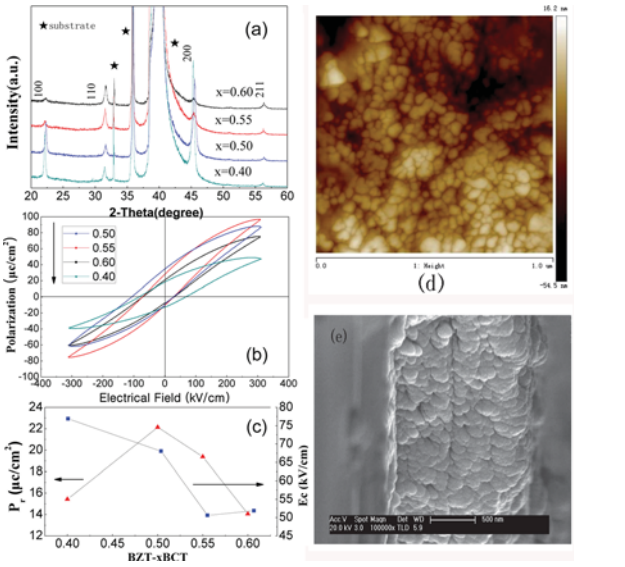

Fig. 9 (a) XRD pattern of BZT–*x*BCT ($x = 0.40, 0.50, 0.55, 0.60$) thin films (b) *P*–*E* hysteresis loops of the above BZT–*x*BCT series, (c) remnant polarization P_r and coercive field E_c of the same BZT–*x*BCT series. (d) AFM topographic images of the surface of BZT–0.5BCT thin film annealed at 850 °C, (e) morphology of the cross section of BZT–0.5BCT thin film annealed at 850 °C.

between the reactants is maximized by such geometry. Such a structure also provides atomic level contact between the metal ions, thus resulting in promoted diffusion of $Ba^{2+}(Ca^{2+})$ within the Ti–O–Zr–O– lattice, and prevents the generation of other distinct crystalline phases prior to formation of the BZT–*x*BCT phase. However, inevitably, there are still some particles with a mechanical mixture, and the contact area between the reactants in such a case is much smaller than that in the core–shell particles, and, consequently, most reaction occurs around or near the carbonate decomposition temperature, and probably involves BaO or CaO as an intermediate active species. On the basis of the detailed XRD, Raman, and thermal analyses, the different routes leading to the formation of crystalline BZT–*x*BCT from the gel to ceramic are schematically summarized in Fig. 8.

Ferroelectric properties

Fig. 9(a) shows XRD patterns for the BZT–*x*BCT ($x = 0.40$, 0.50, 0.55, 0.60) thin films annealed at 850 °C, showing that the films had a single-phase pseudo-cubic perovskite structure. The average grain size and thickness of thin films is about 36 nm and 800 nm, respectively, as shown in the AFM image and SEM photographs of Fig. 9(d) and (e). Fig. 9(b) and (c) reveal the composition dependence of the ferroelectric polarization hysteresis loops, remanent polarization P_r and the coercive field E_c of the BZT–*x*BCT thin films. In line with the corresponding ceramic counterpart,[10] all the properties show anomalies around the MPB composition BZT–0.5BCT, such as the highest value of P_r (22.15 μC cm^{-2}) and fairly low E_c (68.06 kV cm^{-1}). The maximum polarization of BZT–0.50BCT thin films may be due to a low energy barrier of the film for polarization rotation and lattice distortion.[47] The coercive field was dramatically higher than the value of 1.68 kV cm^{-1} for the bulk ceramic counterpart.[10] The much higher coercive field came from the much smaller grains in comparison with the bulk ceramic and hence much more grain boundaries in thin film samples, and also the substrate clamping effect.[18] It can be seen in Table 1 that the remnant polarization (P_r) of the BZT–0.5BCT films obtained in our work was slightly higher than the reported data, including BZT–0.5BCT and other non-Pb ferroelectric films. For the polarization measurements, shifts of *P*–*E* hysteresis loops were noted. This phenomenon is known as imprinting and describes the preference of one polarization state over the other, leading to a shift of the ferroelectric hysteresis on the electrical field axes. It is ascribed to the flexoelectric effect in epitaxial ferroelectric thin films, and it can be completely eliminated by applying an optimized external, uniform electric field.[48,49] The shifts in the polarization are due to the asymmetry of the top and bottom electrode.

Table 1 Comparison of P_r and E_c among BZT–0.5BCT and other non-Pb ferroelectric films

Material	Ref.	P_r (μC cm^{-2})	E_c (kV cm^{-1})
BZT–*x*BCT	Ceramic (ref. 10)	18	1.68
	Film1 (ref. 17)	14.1	17.7
	Film2 (ref. 18)	15.8	58
	This work	22.15	68
KNN	Film3 (ref. 50)	16.4	42
NBT–*x*KBT	Film4 (ref. 51)	13.2	>100
NBT–BT–KNN	Film5 (ref. 52)	20	40.4
BNT	Film6 (ref. 53)	8.3	200

Conclusions

In summary, BZT–*x*BCT ferroelectric thin films were deposited on Pt/Ti/SiO_2/Si substrates using a wet chemical solution approach. Fine, uniform thin films with a single perovskite structure phase were obtained. Among the different compositions of BZT–*x*BCT studied in this paper, BZT–0.5BCT thin films showed the highest remnant polarization of 22.15 μC cm^{-2} and a relative lower coercive field of 68.06 kV cm^{-1}, showing MPB features. By using FTIR/XRD/Raman/DSC-TG techniques, the structure and constituent evolution of the BZT–0.5BCT gels as they nucleate and grow from an amorphous metallorganic gel under ultrabenign conditions were investigated; it is found that the continuous formation of BZT–0.5BCT occurs over the calcination temperature range 550–850 °C. A possible BZT–0.5BCT formation mechanism may be identified as both core–shell particle structures in the gel matrix and mechanical mixture routes, which was deduced by a much lower starting formation temperature, together with the retention behaviors of anion species encapsulated in the gel matrix. The local atom structure studied by Raman spectra revealed that the degree of tetragonal phase during the reaction grows higher and higher with the increase of sintering temperature in BZT–0.5BCT, also showing the characteristic ferroelectric–ferroelectric phase transition going through the MPB for BZT–*x*BCT.

Acknowledgements

This work is financially sponsored in part by the National Basic Research Program of China (Grant no. 2012CB619401), the Key Program of the National Natural Science Foundation of China (Grants no. 11134004), the Natural Science Foundation of China (Grants no. 51002029), the Doctoral Fund of Ministry of Education of China (no. 20100092120039) and the Opening project for the State Key Laboratory of Crystal Materials, Shandong University, P. R. China (Grant no. KF1107). The authors also thank the Analysis and Testing Centre of Southeast University of China for the DSC-TG (STA449 F3) and FESEM (FEI, XL30) analysis.

Notes and references

1 K. Uchino, *Ferroelectric Devices*, Marcel Dekker, New York, 2000, ch. 7.
2 B. Jaffe, *Piezoelectric Ceramics*, Academic Press, New York, 1971, ch. 7.
3 T. R. Shrout and S. J. Zhang, *J. Electroceram.*, 2007, **19**, 111.
4 Y. Saito, H. Takao, T. Tani, T. Nonoyama, K. Takatori, T. Homma, T. Nagaya and M. Nakamura, *Nature*, 2004, **432**, 84.
5 X. B. Ren, *Nat. Mater.*, 2004, **3**, 91.

6 M. D. Maeder, D. Damjanovic and N. Setter, *J. Electroceram.*, 2004, **13**, 385.
7 L. Y. Li and X. G. Tang, *Mater. Chem. Phys.*, 2009, **115**, 507.
8 X. G. Tang, K. H. Chew and H. L. W. Chan, *Acta Mater.*, 2004, **52**, 5177.
9 Q. X. Liu, X. G. Tang, Y. Y. Deng, J. Wang and H. L. W. Chan, *Mater. Chem. Phys.*, 2008, **112**, 281.
10 W. F. Liu and X. B. Ren, *Phys. Rev. Lett.*, 2009, **103**, 257602.
11 H. X. Bao, C. Zhou, D. Z. Xue, J. H. Gao and X. B. Ren, *J. Phys. D: Appl. Phys.*, 2010, **43**, 465401.
12 D. Z. Xue, Y. M. Zhou, H. X. Bao, C. Zhou, J. H. Gao and X. B. Ren, *J. Phys. D: Appl. Phys.*, 2011, **109**, 054110.
13 D. Z. Xue, Y. M. Zhou, H. X. Bao, C. Zhou, J. H. Gao and X. B. Ren, *Appl. Phys. Lett.*, 2011, **99**, 122901.
14 J. H. Gao, D. Z. Xue, Y. Wang, D. Wang, L. X. Zhang, H. J. Wu, S. W. Guo, H. X. Bao, C. Zhou, W. F. Liu, S. Hou, G. Xiao and X. B. Ren, *Appl. Phys. Lett.*, 2011, **99**, 092901.
15 J. G. Hao, W. F. Bai, W. Li and J. W. Zhai, *J. Am. Ceram. Soc.*, 2012, 1–9.
16 Y. T. Lin, G. H. Wu, N. Qin and D. H. Bao, *Thin Solid Films*, 2012, **520**, 2800.
17 A. Piorra, A. Petraru, H. Kohlstedt, M. Wuttig and E. Quandt, *J. Appl. Phys.*, 2011, **109**, 104101.
18 G. Q. Kang, K. Yao and J. Wang, *J. Am. Ceram. Soc.*, 2012, **95**, 986.
19 H. S. Gopalakrishnamurthy, M. S. Rao and T. R. N. Kutty, *J. Inorg. Nucl. Chem.*, 1975, **37**, 891.
20 S. Kumar, G. L. Messing and W. B. White, *J. Am. Ceram. Soc.*, 1993, **76**, 617.
21 W. S. Cho, *J. Phys. Chem. Solids*, 1998, **59**, 659.
22 X. Xing, J. Deng, J. Chen and G. Liu, *J. Alloys Compd.*, 2004, **384**, 312.
23 C. Sanchez, J. Livage, M. Henry and F. Babonneau, *J. Non-Cryst. Solids*, 1988, **100**, 65.
24 G. Monros, J. Carda, M. A. Tena, P. Eribano, M. Sales and J. Alarcon, *J. Non-Cryst. Solids*, 1992, **147**, 588.
25 K. Holland-Moritz, In *Fourier Transform Infrared Characterization of Polymers*, ed. H. Ishida, Plenum Press, New York, 1987, p. 190.
26 B. George and P. McIntype, *Infrared Spectroscopy*, John Wiley & Sons, Chichester, 1987, p 312.
27 A. L. Smith, *Applied Infrared Spectroscopy*, John Wiley & Sons, New York, 1979, p 288.
28 M. T. Buscaglia, V. Buscaglia and R. Alessio, *Chem. Mater.*, 2007, **19**, 711.
29 Y. Shiratori, C. Pithan, J. Dornseiffer and R. Waser, *J. Raman Spectrosc.*, 2007, **38**, 1288.
30 K. Page, T. Proffen, M. Niederberger and R. Seshadri, *Chem. Mater.*, 2010, **22**, 4386.
31 R. Asiaie, W. Zhu, S. A. Akbar and P. K. Dutta, *Chem. Mater.*, 1996, **8**, 226.
32 F. A. Rabuffetti and R. L. Brutchey, *J. Am. Chem. Soc.*, 2012, **134**, 9475.
33 P. K. Dutta, P. K. Gallagher and J. Twu, *Chem. Mater.*, 1993, **5**, 1739.
34 Y. Shiratori, C. Pithan, J. Dornseiffer and R. Waser, *J. Raman Spectrosc.*, 2007, **38**, 1288.
35 A. Scalabrin, A. S. Chaves, D. S. Shim and S. P. S. Porto, *Phys. Status Solidi B*, 1977, **79**, 731.
36 G. Busca, V. Buscaglia, M. Leoni and P. Nanni, *Chem. Mater.*, 1994, **6**, 955.
37 L. H. Robins, D. L. Kaiser, L. D. Rotter, P. K. Schenck, G. T. Stauf and D. Rytz, *J. Appl. Phys.*, 1994, **76**, 7487.
38 T. C. Huang, M. T. Wang, H. S. Sheu and W. F. Hsieh, *J. Phys.: Condens. Matter*, 2007, **19**, 476212.
39 R. Asiaie, W. Zhu, S. A. Akbar and P. K. Dutta, *Chem. Mater.*, 1996, **8**, 226.
40 M. L. Mngdal, G. P. Mambrini, D. P. Volanti, E. R. Leite, M. O. Orlandi, P. S. Pizani, V. R. Mastelaro, C. O. Paiva-Santos, E. Longo and J. A. Varela, *Chem. Mater.*, 2008, **20**, 5381.
41 Y. Shiratori, C. Pithan, J. Dornseiffer and R. Waser, *J. Raman Spectrosc.*, 2007, **38**, 1288.
42 E. Buixaderas, D. Nuzhnyy, J. Petzelt, L. Jin and D. Damjanovic, *Phys. Rev. B: Condens. Matter Mater. Phys.*, 2011, **84**, 184302.
43 J. F. Scott, *Rev. Mod. Phys.*, 1974, **46**, 83.
44 M. T. Buscaglia, V. Buscaglia, L. Curecheriu, P. Postolache, L. Mitoseriu, A. C. Ianculescu, B. S. Vasile, Z. Zhao and P. Nanni, *Chem. Mater.*, 2010, **22**, 4740.
45 M. T. Buscaglia, V. Buscaglia and R. Alessio, *J. Am. Ceram. Soc.*, 2005, **88**, 2374.
46 A. Motnyk, S. Senz and D. Hesse, *Solid State Ionics*, 2006, **177**, 429.
47 L. H. Robins, D. L. Kaiser, L. D. Rotter, P. K. Schenck, G. T. Stauf and D. Rytz, *J. Appl. Phys.*, 1994, **76**, 7487.
48 J. W. Hong and D. Vanderbilt, *Phys. Rev. B: Condens. Matter Mater. Phys.*, 2011, **84**, 180101.
49 H. Zhou, J. W. Hong, Y. H. Zhang, F. X. Li, Y. M. Pei and D. N. Fang, *Europhys. Lett.*, 2012, **99**, 47003.
50 L. Y. Wang, K. Yao and W. Ren, *Appl. Phys. Lett.*, 2008, **93**, 092903.
51 H. Dong, X. J. Zheng, W. Li, Y. Q. Gong, J. F. Peng and Z. Zhu, *J. Appl. Phys.*, 2011, **110**, 124109.
52 G. Q. Kang, K. Yao and J. Wang, *J. Am. Ceram. Soc.*, 2011, **94**, 1331.
53 T. Yu, K. W. Kwok and H. L. W. Chan, *Thin Solid Films*, 2007, **515**, 3563.

